CrystEngComm

Accepted Manuscript

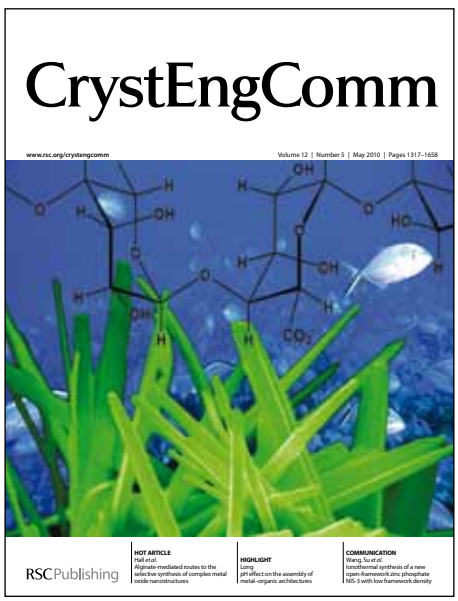

Controllable growth of ZnO/ZnSe heterostructures for visible-light photocatalysis

W. Chen[a,*], N. Zhang[a, b,*], M. Y. Zhang[a,†], X. T. Zhang[a], H. Gao[a,†] , and J. Wen[a]

[a] *Key Laboratory for Photonic and Electronic Bandgap Materials, Ministry of Education，School of Physics and Electronic Engineering, Harbin Normal University, Harbin 150025, P. R. China.*

[b] *College of Chemistry, Jilin University, Changchun, 130012, P. R. China.*

One-dimensional ZnO-core/ZnSe-shell heterostructures with different ratios of the two components were fabricated via a two-step chemical vapor deposition process under the different temperatures of the substrates. The scanning electron microscopy images show that the numerous ZnSe nanoparticles with different sizes are uniformly distributed on the surface of ZnO nanobelts. The X-ray diffraction patterns confirm that the heterostructures are composed of wurtzite ZnO and cubic ZnSe. The intensity ratios of the visible emissions to ultraviolet emission from 0.15 to 14.50 are tuned by the change of the component due to the type-II energy band alignment structure. The photoluminescence mechanism of the ZnO/ZnSe heterostructures is proposed. In addition, the absorption of ZnO/ZnSe heterostructures extends from the ultraviolet region to the visible region, compared with the pure ZnO. The ZnO/ZnSe heterostructures with type-II energy band alignment show a high photocatalytic activity.

Key Words:

ZnO/ZnSe; Heterostructures; One-dimensional; Type-II energy band; Visible-light photocatalysis

* These authors contributed equally to this work.
† *Corresponding Author E-mails: mysci@foxmail.com and gaohong65cn@126.com*

In the past few decades, one dimensional (1D) semiconductor nanostructures have attracted tremendous attention owing to their potential applications in nano-optoelectronics. [1-12] Recently, 1D heterostructures are gaining increasingly research interest because of the possibilities of tuning their electronic, chemical, and optical properties on a large scale, which can lead to the tunable multiple functionalities. [13-20] Significant progress in the synthesis of various 1D heterostructures has been made, which gives us a chance to study the effect of their different components on the optical and electronic properties of the 1D heterostructures.

Nowadays, controlled fabrication of component-modulated heterostructures at the nanoscale is a key factor for tuning the optical properties of the 1D semiconducting heterostructures. As an important II−VI semiconductor, ZnO with direct band gap of ~3.37 eV is appropriate for a variety of applications related to solar cells, sensors, lasers, displays, and nanogenerators. It is well-known that ZnO is also a useful material for photocatalysis. However, ZnO cannot absorb visible-light and thus makes use of only 3-5% of the solar spectrum that reaches the earth due to its wide band-gap. The heterostructure is a promising way to improve the optical absorption capacity. ZnSe is an ideal choice for producing type-II ZnO heterostructures due to its relatively narrow band-gap (2.7 eV). Considerable progress in preparing ZnO/ZnSe heterostructures has been achieved by different techniques during the past decades. [21-23] Very recently ZnO-core/ZnSe-shell nanowire arrays were synthesized via a two-step chemical vapor deposition (CVD) method by Wu et al. [24] However, how to

obtain the heterostructures with tunable proportion of ingredients is a challenge for various synthesis technologies. Moreover the investigations on the optical and catalytic properties of ZnO/ZnSe heterostructure are quite rare.

In this paper, different component ratios of ZnO to ZnSe for their heterostructures were controllably synthesized by a two-step CVD process, varying the temperature of the substrate. Their optical properties were studied by photoluminescence (PL) and absorption spectra. These results indicate that ZnO/ZnSe heterostructures can provide an effective way to the separation of photogenerated electron-hole pairs and utilize the visible light for photocatalysis. The ZnO/ZnSe heterostructures display an efficient photoactivity for the degradation of organic pollutants and can be easily recycled for reuse.

The ZnO/ZnSe heterostructures were synthesized by a two-step CVD process. First, synthesis of ZnO nanobelts: the ZnO powder was loaded into one end of an alumina boat as the source materials. Si wafers with a thin film of Au, of ~2 nm coverage, placed the downstream of the precursor. The furnace was heated to a preset temperature (1350 ^{o}C) and maintained at this temperature for 30 min. Pure N_2 as carrier gas flowed into the alumina tube at a flow rate of 100 sccm and a pressure of 1000 Pa. And then, the system was cooled down naturally to the ambient temperature.

Second, synthesis of ZnO/ZnSe heterostructures: The ZnSe powder was loaded into one end of an alumina boat. The as-synthesized ZnO nanobelts, which were labeled as ZSH0, were then used as templates placing the downstream of the precursor. The individual templates were located at different growth temperatures. The furnace

was heated to a preset temperature (950 ^{o}C) and maintained for 1 h under the same experimental conditions. ZnO/ZnSe heterostructures obtained at different growth temperatures from low to high were labeled as ZSH1 (~600 ^{o}C), ZSH2 (~650 ^{o}C), and ZSH3 (~700 ^{o}C), respectively.

The morphology and chemical composition of the as-synthesized ZnO nanobelts and ZnO/ZnSe heterostructures were characterized by field-emission scanning electron microscopy (FE-SEM; S-4800, Hitachi, Japan) equipped with energy dispersive x-ray (EDX) spectrometer. The crystalline structure of the ZnO/ZnSe heterostructure was characterized by x-ray powder diffraction (XRD, D/max2600, Rigaku, Japan) and transmission electron microscopy (TEM; FEI, Tecnai TF20). UV-vis diffuse reflectance spectra (DRS) of the samples were obtained by using a UV–vis spectrometer (Perkin–Elmer, Lambda 850) used polytetrafluoroethylene (PTFE) as a reference and then they were converted to absorbance by the Kubelka–Munk method. PL spectra were measured using a micro-Raman spectrometer (J-Y, HR800, France), employing the 325 nm line of a He-Cd laser as the excitation light source. Similar to the experiment published previously, [25] the as-synthesized nanofilms (~0.5 cm^2) of ZnO/ZnSe heterostructures were threw into 5 mL Rhodamine B (RhB) aqueous solutions with each of the concentration is 1.0 × 10^{-5} M, and the amount of ZnO/ZnSe heterostructures catalyst used was l.5 mg. The solution was irradiated using a 300 W Xe lamp (10 cm away from the suspension) at room temperature, and the illuminant wavelength filtered by an optical filter starts from 400 nm. All these measurements were made at room temperature.

Fig. 1a shows a typical SEM image of the as-synthesized ZnO nanobelts. The nanobelts have smooth surfaces. Their width is about 300-400 nm while the length does several tens micrometers. Figs. 1b-d exhibit SEM images for ZSH1, ZSH2, and ZSH3, respectively. There are numerous ZnSe nanoparticles on the surface of the ZnO nanobelts. These nanoparticles are uniformly distributed. The insets in Figs.1b-1d are enlarged SEM images of the ZSH1, ZSH2, and ZSH3, respectively. The size and density of nanoparticles for ZSH1, ZSH2, and ZSH3 increase gradually with the increase of the growth temperature.

The EDX spectra in SEM for ZSH1, ZSH2, and ZSH3 are shown in Fig. 2, confirming that all of the products are composed of Zn, O, and Se, and that the ratio of (O+Se) to Zn is close to 1. From the EDX spectra, the component ratios of ZnO to ZnSe are calculated to be (4:1), (1:1), and (1:3), respectively, in sequence.

The XRD patterns of the as-synthesized products are shown in Fig. 3. There are two sets of XRD peaks for ZSH1, ZSH2, and ZSH3 to appear in the pattern except ZSH0. Diffraction peaks from wurtzite structure ZnO (W-ZnO) phase (JCPDS Card No.36-1451) are observed in all the samples. The other diffraction peaks come from cubic structure ZnSe phase (JCPDS Card No.37-1463). The relative intensities of ZnSe peaks for ZSH1, ZSH2, and ZSH3 increase gradually, which is consistent with the amounts of ZnSe existed in the products. No new phase is found, indicating the formation of ZnO-core/ZnSe-shell.

In order to obtain detailed information about the morphology and microstructure of the as-synthesized products, the TEM and high-resolution transmission electron

microscopy (HRTEM) observations are carried out, as shown in Fig. 4. HR-a-d are the corresponding HRTEM images of the ZSH0, ZSH1, ZSH2, and ZSH3 for Figs. 4 a-d, respectively. From HR-a, the lattice fringes of d = 0.28 nm match well with the $(10\bar{1}0)$ crystal planes of wurtzite ZnO. Fig. 4b clearly demonstrates that the nanoparticles with the dimensions in the range of several nanometers to tens nanometers are uniformly distributed on the surface of the ZnO nanobelts. The ZnSe nanoparticles have an irregular shape. The interplanar distance is 0.33 nm that is consistent with the (111) crystal plane of cubic ZnSe. Figs.4c and 4d further confirm that the size and density of ZnSe nanoparticles increase with the increase of the ZnSe content.

To clarify the composition distribution of the product and structure properties, the spatial distribution of the compositional elements within the heterostructures was obtained by using TEM-EDX line scans along the nanobelt's radial direction (marked by the red line in the inset of Figure 5). There are three signal peaks of Zn, O, and Se, as shown in Fig. 5. The O signal is mainly confined within the ZnO core area, while a higher intensity of Se is found in the shell region. Zn signal appears within the core and the shell. This is consistent with the ZnO-core/ZnSe-shell nanobelt configuration observed in the TEM image. The ZnO core has a single-crystal wurtzite structure, which can be confirmed by the high resolution image taken from the same nanobelt (Figure. 4b). The ZnSe shell is polycrystalline with a cubic structure based on the random dispersion for ZnSe nanoparticles on the surface of a ZnO nanobelts and the selected area electron diffraction pattern (not show).

The UV-vis absorption spectra of the ZSH0, ZSH1, ZSH2, and ZSH3 are shown

in Fig. 6a. The absorption spectra reveal significant differences in the optical absorption properties of the ZnO nanostructures and the ZnO/ZnSe heterostructures. The ZSH0 shows strong absorption in the ultraviolet region, which is a characteristic of the wide band-gap ZnO semiconductor materials. However, the absorption gradually extends from ultraviolet to visible region and enhances in intensity with the increase of the ZnSe component. A typical derivative-curve of the reflectance spectrum for ZSH2 is shown in Fig. 6b in order to clearly observe the absorption peak. From Fig. 6b, a new absorption peak at 2.1 eV is found except near-band-edge (NBE) absorption peaks from ZnO and ZnSe.

To study the luminescent properties of the ZnSe/ZnO heterostructures, the PL measurements were carried out by a He -Cd laser, using line of 325 nm as excitation wavelength at room temperature, as shown in Fig. 7. All PL spectra consist of ultraviolet emission peak and visible emission bands. We are interested in the visible emission bands and the relative peak intensity of ZnO, and fit the visible emission bands of the ZSH1, ZSH2, and ZSH3 by Multi-peak Gaussian, as shown the blue and pink lines in Fig. 7. Together with the fitting results, there are three peaks centered at 3.25 eV, 2.31 eV, and 2.0 eV, respectively, in the PL spectrum for ZSH1. For ZSH2, the four peaks are located at 3.25 eV, 2.7 eV, 2.31 eV, and 2.0 eV, respectively. For ZSH3, the four peaks are centered at 3.25 eV, 2.7 eV, 2.31, eV and 2.0 eV, respectively. As is well known, the ultraviolet emission peak at 3.25 eV belongs to the NBE emission of ZnO, [26, 27] while the emission at about 2.31 eV is associated with defect emission of ZnO. [28] The peak at 2.7 eV is ascribed to the NBE emission of ZnSe, [29]

while the visible emission bands centered at about 2.0 eV may be mainly attributed to the interfacial transitions between ZnO and ZnSe due to the stocks shift (see below in the text). Based on the above information gathered, the intensity ratios of the visible emission to the NBE emission for ZnO in ZSH1, ZSH2, and ZSH3 are 0.15, 0.70 to 14.50. The possible reasons will be analyzed below.

The energy band structure diagram of ZnO/ZnSe heterostructures is depicted, as shown in Fig. 8. Fig. 8a is the diagram of the ZnO structure and ZnSe structure before energy band alignment, the diagram is drawn by using the vacuum level as the standard, the electron affinities for ZnO and ZnSe are taken as 4.35 eV [30] and 4.09 eV [31], respectively. Fig. 8b is the diagram of the ZnO structure and ZnSe structure after energy band alignment. The effective bandgap (Eg_{eff}) of the ZnO/ZnSe heterostructures is obtained to be 1.69 eV by first principle calculation. [32] However, it is about 2.1 eV by UV-vis absorption spectrum (Fig. 6b). The above PL phenomenon observed for ZnO/ZnSe heterostructures can be ascribed to the four possible reasons: (i) photogenerated holes in the valence band of ZnO could transfer to the valence band of ZnSe due to the type-II energy band, as shown in Fig. 8b, which makes its hole concentration become low and the charge between the ZnO and ZnSe separate, resulting in the weakening of PL from the NBE of ZnO core. In addition, more photogenerated holes in the valence band of ZnO will transfer to that of ZnSe with the increase of ZnSe component or the interface between the core and shell, leading to a weaker PL from the NBE of ZnO and a more intense PL from the NBE of ZnSe; (ii) the emitted photons from the NBE of ZnO core can be absorbed by ZnSe shell; (iii)

the electrons in the conduction band of ZnO transit to the valence band of ZnSe at the interface; (iv) non-radiative recombination can happen at their interface due to the interfacial defects. So, we can conclude that the type-II band alignment for the ZnO/ZnSe heterostructures can efficiently separate photo-generated carriers [24] and they could have high photocatalytic activities.

To demonstrate the photoactivity of the as-synthesized ZnO/ZnSe heterostructures for the degradation of organic pollutants, experiments for the photocatalytic degradation of RB as a test reaction were carried out under visible-light irradiation from a 300 W Xe lamp using a UV cutoff filter (>400 nm). RB was selected as a model pollutant because it is a common contaminant in industrial wastewater and has good resistance to light degradation. What's more, RB cannot be photodegraded in the absence of any photocatalyst under visible-light irradiation. In the experiments, pure ZnO nanobelts were used as a photocatalytic reference to study the photocatalytic activity of the ZnO/ZnSe heterostructures. As shown in Fig. 9, when no photocatalyst is present, the degradation of the RB is extremely slow—only 6% of the RB is decolorized after 9 h of irradiation. Meanwhile, pure ZnO nanobelts exhibit that negligible activity and the photodegradation efficiency of RB just reach about 71% after 9 h of reaction, which can be attributed to the photosensitization from RB molecule. In comparison, the degradation efficiencies of RB are about 96, 95, and 92% for the ZSH1, ZSH2 and ZSH3, respectively. Obviously, the ZnO/ZnSe heterostructures show much higher photocatalytic activities than that of pure ZnO nanobelts.

The enhanced photocatalytic performance of ZnO/ZnSe heterostructure is due to the following factors: firstly, according to DRS analysis, the samples ZSH1, ZSH2 and ZSH3 exhibit enhanced visible-light absorption. It is evident from the results that ZnO/ZnSe heterostructures absorb more visible light than pure ZnO and thus display better photocatalytic activity. However, the photocatalytic activity of ZSH3 do not show dramatically increase when the content of the ZnSe is further increased, although the visible-light absorption is enhanced, indicating that the enhanced visible-light absorption is not the only factor influencing the activity of the heterostructures. Secondly, the molar ratios of ZnO to ZnSe also affect the photocatalytic activity. The superior reactivity of the ZnO/ZnSe heterostructures is observed with appropriate molar ratios of ZnO to ZnSe, suggesting that there is a critical ratio for such a positive synergistic effect. Above this critical ratio, excessive ZnSe covers the active sites of ZnO and hinders the electron transfer on the interfaces of ZnO/ZnSe heterostructure nanobelts, and thus in turn inhibit the photoactivity. Last but not least, the presence of heterojunction in the ZnO/ZnSe heterostructures may also improve the composite activity, which favors the separation of photogenerated electrons-holes pairs in the ZnO/ZnSe heterostructures. In this work, the as-adopted fabrication route is successful to realize a close contact of ZnSe nanoparticles with ZnO nanobelts in ZnO/ZnSe heterostructures, as evidenced by SEM and TEM observation above. Such close contact is more effective in suppression of the electron-hole recombination.

Moreover, cycling uses as well as maintaining high photocatalytic activity is a

critical issue for long-term use in practical applications of the catalyst. In this work, the samples are of two-dimensional nanofilms morphology and can be easily separated from an aqueous suspension. It is indicated that the ZnO/ZnSe heterostructure displays an efficient photoactivity for the degradation of organic pollutants and can easily be recycled for reuse.

In summary, ZnO/ZnSe heterostructures with different ratios of ZnO to ZnSe are successfully synthesized via a two-step CVD process by varying the temperature of the substrates. The density of ZnSe nanoparticles affects the PL and catalysis properties of the ZnO/ZnSe heterostructures. The relative intensity of visible emissions to the ultraviolet emission become larger with the increase of the density for ZnSe component, due to the type-II energy band structure, while the photocatalytic activities of the ZnO/ZnSe heterostructures do higher, due to the positive synergistic effect of photosensitization and photocatalytic. This study will give us some inspiration to synthesize different rates of component heterostructures and to control the optical properties and the visible photocatalytic activity.

Acknowledgments

This work was partially supported by the Natural Science Foundation of China (No. 51172058 and 11074060), the Key Project of Natural Science Foundation of Heilongjiang Province (ZD201112), and Institution of Higher Education, Doctoral Fund Jointly Funded Project (20112329110001), and the Graduate Students' Scientific Research Innovation Project of Heilongjiang Province (YJSCX2012-186HLJ).

References:

1 Q. Ahsanulhaq, J. H. Kim, J. S. Lee and Y. B. Hahn, *Electrochem. Commun.*, 2010, **12**, 475.

2 Y. F. Lin, T. H. Chen, C. H. Chang, Y. W. Chang, Y. Cheng, Y. C. Chiu, H. C. Hung, J. J. Kai, Z. P. Liu, J. Fang and W. B. Jian, *Phys. Chem. Chem. Phys.*, 2010, **12**, 10928.

3 X. T. Zhang, K. M. Ip, Q. Li and S. K. Hark, *Appl. Phys. Lett*., 2005, **86**, 203114.

4 H. Y. Xu, Z. Liu, X. T. Zhang and S. K. Hark, *Appl. Phys. Lett.*, 2007, **90**, 113105.

5 S. Y. Bae, C. W. Na, J. H. Kang and J. Park, *J. Phys. Chem. B.*, 2005, **109**, 2526.

6 L. Shi, C. Pei, Y. M. Xu and Q. Li, *J. Am. Chem. Soc.*, 2011, **133**, 10328.

7 R. Ullah and J. Dutta, *J. Hazard. Mater.*, 2008, **156**, 194.

8 S. S. Ma, R. Li, C. P. Lv, W. Xu and X. L. Gou, *J. Hazard. Mater.*, 2011, **192**, 730.

9 C. Soci, A. Zhang, B. Xiang, S. A. Dayeh, D. P. R. Aplin, J. Park, X. Y. Bao, Y. H. Lo and D. Wang, *Nano Lett.*, 2007, **7**, 1003.

10 Y. P. Leung, W. C. H. Choy and T. I. Yuk, *Chem. Phys. Lett.*, 2008, **457**, 198.

11 C. H. Li, J. A. Zapien, Y. Yao, X. M. Meng, C. S. Lee, S. S. Fan, Y. Lifshitz and S. T. Lee, *Adv. Mater.*, 2003, **15**, 838.

12 L. Shi, A. J. T. Naik, J. B. M. Goodall, C. Tighe, R. Gruar, R. Binions, I. Parkin and J. Datt, *Langmuir*, 2013, **29**, 10603.

13 L. Xu, R. F. Zheng, S. H. Liu, J. Song, J. S. Chen, B. Dong and H. W. Song, *Inorg. Chem*., 2012, **51**, 7733.

14 M. Y. Zhang, C. L. Shao, J. B. Mu, Z. Y. Zhang, Z. C. Guo, P. Zhang and Y. C. Liu, *CrystEngComm*., 2012, **14**, 605.

15 X. Zhang, X. H. Li, C. L Shao, J. H. Li, M. Y. Zhang, P. Zhang, K. X. Wang, N. Lu

and Y. C. Liu, *J. Hazard. Mater.*, 2013, **260**, 892.

16 X. T. Zhang, M. L. Chen, J. Wen, L. L. Wu, H. Gao and D. Zhang, *CrystEngComm*., 2013, **15**, 1908.

17 S. K. Chong, C. F. Dee and S. A. *Nanoscal. Res. Lett*., 2013, **8**, 174.

18 N. K. Reddy, M. Devika, N. Shpaisman, M. B. Ishai and F. Patolsky, *J. Mater. Chem*., 2011, **21**, 3858.

19 J. S. Lee, O. S. Kwon and J. Jang, *J. Mater. Chem*., 2012, **22**, 14565.

20 J. Xu, X. Yang, H. K.Wang, X. Chen, C. Y. Luan, Z. X. Xu, Z. Z. Lu, V. A. L. Royl, W. J. Zhang and C. S. Lee, *Nano Lett*., 2011, **11**, 4138.

21 S. Cho, J. W. Jang, J. Kim, J. S. Lee, W. Y. Choi and K. H. Lee, *Langmuir.*, 2011, **27**, 10243.

22 J. Xu, X. Yang, Q. D. Yang, T. L.Wong, S. T. Lee, W. J. Zhang and C. S. Lee, *J. Mater. Chem.*, 2012, **22**, 13374.

23 L. H. Zhang, H. Q. Yang and L. Li, *Mater. Chem. Phys.*, 2010, **120**, 526.

24 Z. M. Wu, Y. Zhang, J. J. Zheng, X. G. Lin, X. H. Chen, B. W. Huang, H. Q. Wang, K. Huang, S. P. Li and J. Y. Kang, *J. Mater. Chem.*, 2011, **21**, 6020.

25 K. Natarajan, T. S. Natarajan, H.C. Bajaj and R. J. Tayade, *Chem. Eng. J.*, 2011, **178,** 40.

26 P. Wang, X. T. Zhang, J. Wen, L. L.Wu, H. Gao, E. Zhang and G. Q. Miao, *J. Alloy. Compd.*, 2012, **533**, 88.

27 X. Liu, X. H. Wu, H. Cao and R. P. H. Chang, *J. Appl. Phys.*, 2004, **95**, 3141.

28 H. M. Hu, C. H. Deng and X. H. Huang, *Mater. Chem. Phys.*, 2010, **121**, 364.

29 X. T. Zhang, K. M. Ip, Z. Liu, Y. P. Leung, Q. Li and S. K. Hark, *Appl. Phys. Lett.* , 2004, **84**, 2641.

30 Y. I. Alivov, E. V. Kalinina, A. E. Cherenkov, D. C. Look and B. M. Ataev, *Appl. Phys. Lett.*, 2003, **83**, 4719.

31 J. Ihm and M. L.Cohen, *Phys. Rev. B.*, 1979, **20**, 729.

32 J. C. Ni, Z. M. Wu, X. G. Lin, J. J. Zheng, S. P. Li, J. Li and J. Y. Kang, *J. Mater. Res.*, 2012, **27**, 730.

Figure Captions:

Figure 1. SEM images of (a) ZSH0, (b) ZSH1, (c) ZSH2, and (d) ZSH3. Insets in (b), (c), and (d) are high-magnification SEM images of a single ZSH1, ZSH2, and ZSH3, respectively.

Figure 2. EDX spectra of all the heterostructures.

Figure 3. XRD patterns of ZSH0, ZSH1, ZSH2, and ZSH3.

Figure 4. (a-d) Low-magnification TEM images of ZSH0, ZSH1, ZSH2, and ZSH3, respectively. (HR-a-d) Corresponding HRTEM images as marked by red square in (a)-(d), respectively.

Figure 5. A representative EDX line scanning spectroscopy for a single heterostructure (inset) of ZSH2.

Figure 6. (a) UV-vis absorption spectra of ZSH0, ZSH1, ZSH2, and ZSH3. (b) The derivative cure of the ZSH2. An absorption peak at 2.1 eV is observed except NBE absorption peaks from ZnO and ZnSe.

Figure 7. The black curves are PL spectra of ZSH1, ZSH2, and ZSH3 at room temperature, the pink and blue curves are the fitting results of PL spectra of ZSH1, ZSH2, and ZSH3.

Figure 8. Schematic diagrams show the energy band structure of ZnO and ZnSe before and after alignment, respectively, and the possible charge transfer process, employing the 325 nm line of a He-Cd laser as the excitation light source.

Figure 9. Photocatalytic degradation of ZSH0, ZSH1, ZSH2, and ZSH3 under visible-light illumination.

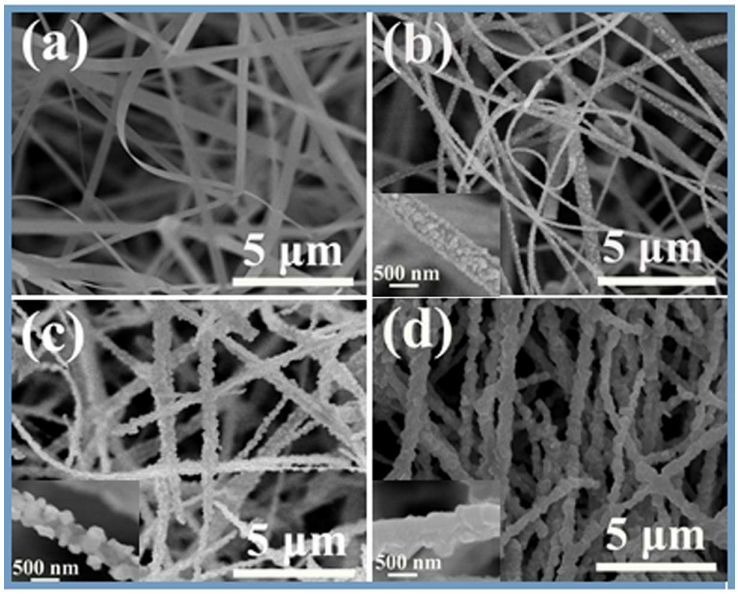

Figure 1 by W. Chen, et al..

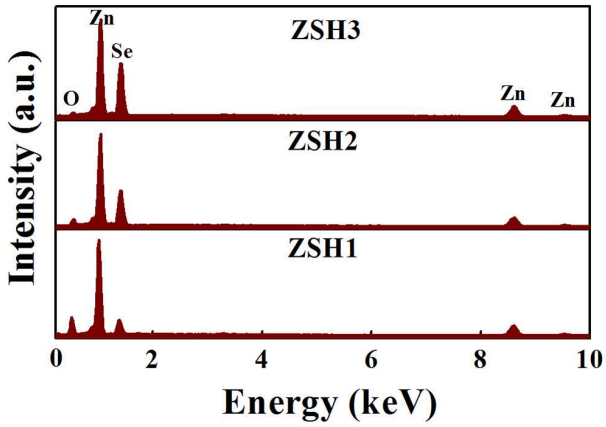

Figure 2 by W. Chen, et al..

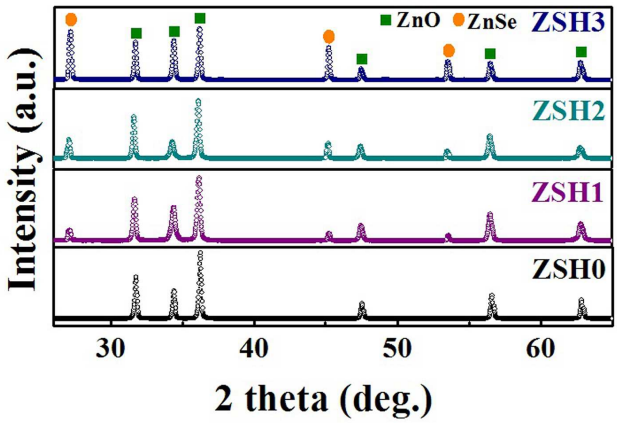

Figure 3 by W. Chen, et al..

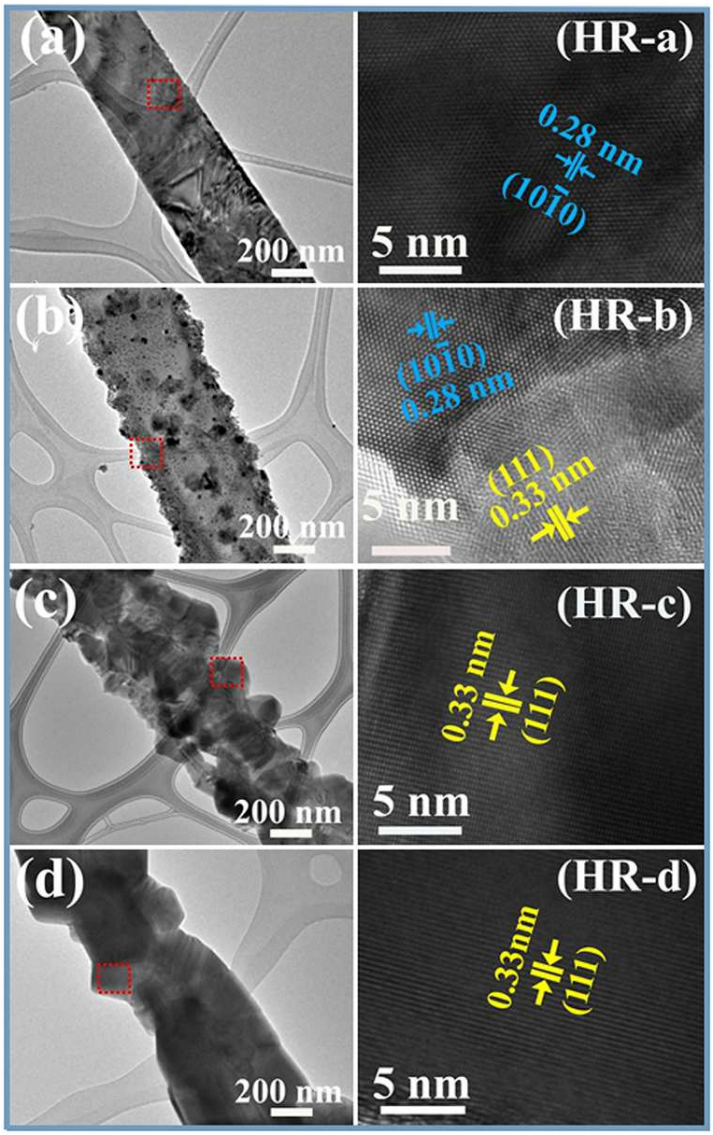

Figure 4 by W. Chen, et al..

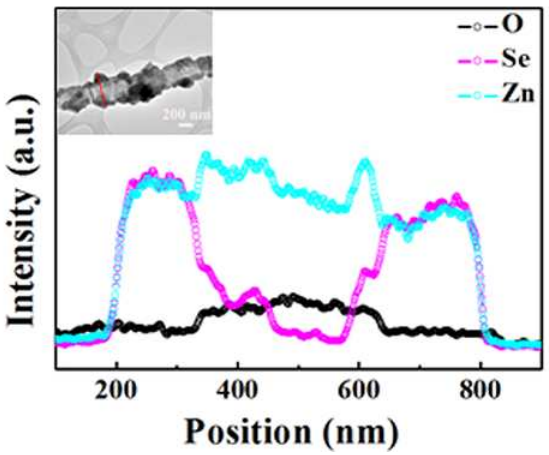

Figure 5 by W. Chen, et al..

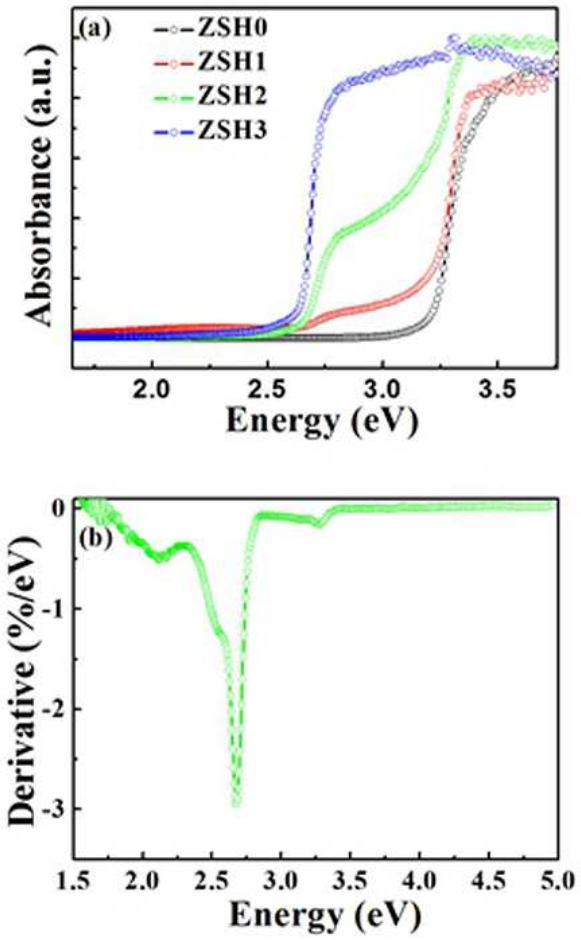

Figure 6 by W. Chen, et al..

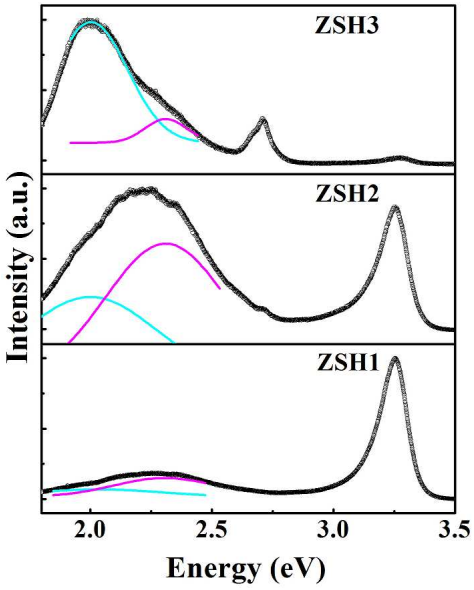

Figure 7 by W. Chen, et al..

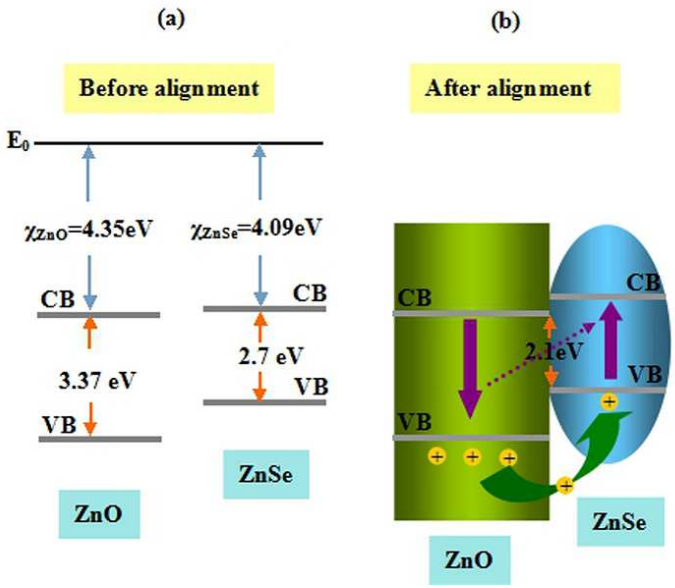

Figure 8 by W. Chen, et al..

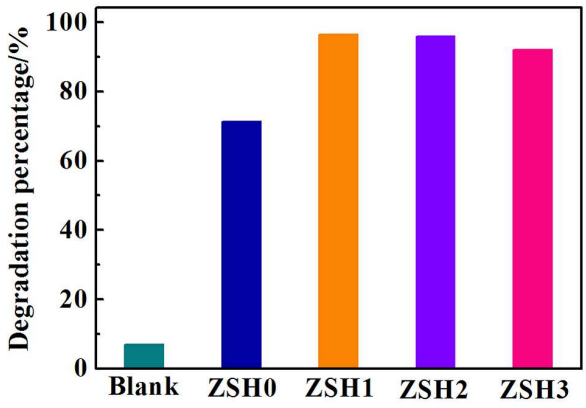

Figure 9 by W. Chen, et al..

Table of contents

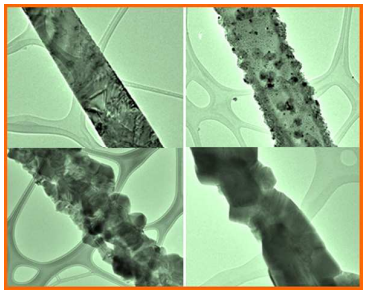

ZnO/ZnSe heterostructures for visible-light photocatalysis are fabricated via a two-step CVD process.